

# Tool for Rapid Transient Transpiration Cooled Re-Entry Simulation

Tobias Hermann<sup>\*</sup>, Imran Naved<sup>†</sup> and Matthew McGilvray<sup>‡</sup>

*The University of Oxford, Department of Engineering, Osney Mead, Southwell Building, Oxford OX2 0ES, United Kingdom*

This paper presents a numerical model intended for a system study of transpiration cooled thermal protection systems. The code PIRATE (Porous Impulse Response Analysis for Transpiration cooling Evaluation) enables rapid transient calculations for thermal protection systems of hypersonic flight vehicles. In the code, semi-empirical aerodynamic correlations are employed. However, the code could also be used by applying higher fidelity inputs from CFD calculations for more complicated vehicle geometries. The wall temperature distribution is calculated by utilising the thermal impulse and step responses of porous media, increasing the calculation speed significantly. A heat flux balance is considered for a one-dimensional porous material. The code is validated with experimental data of plasma wind tunnel tests and the SHEFEX II flight experiment. The transient heating of a flat plate model in a steady state flow condition in the L2K plasma wind tunnel is assessed for both un-cooled and transpiration cooled cases. The SHEFEX II flight simulation accounts for transient external flow conditions and is used to assess the downstream coolant film effect after the injection point. The trends of experimental temperature measurements are replicated well by the simulations. The predicted and measured temperatures are in good agreement and within a margin of 10 % with maximum deviations of 40 K.

## Nomenclature

$A$	=	Parameter of Lee's model
$A$	=	Parameter in Van Driest's model
$A_i$	=	Parameter of thermal model
$A_s$	=	Surface area, m <sup>2</sup>
$B$	=	Parameter of Lee's model
$B$	=	Parameter in Van Driest's model

---

<sup>\*</sup>Post-doctoral research assistant, Hypersonics group, Oxford Thermofluids Institute, AIAA Member.

<sup>†</sup>DPhil student, Hypersonics group, Oxford Thermofluids Institute, AIAA Member.

<sup>‡</sup>Associate Professor, Hypersonics group, Oxford Thermofluids Institute, AIAA Member.

$B_h$	=	Blowing parameter
$b$	=	Depth within material, m
$B_i$	=	Parameter of thermal model
$C_i$	=	Parameter of thermal model
$c_p$	=	Specific heat capacity, $\text{J kg}^{-1} \text{K}^{-1}$
$D$	=	Heat flux parameter of Lee's model
$F$	=	Blowing ratio $(\rho_f u_f)/(\rho_g u_g)$
$h$	=	Specific enthalpy, $\text{J kg}^{-1}$
$H_{\text{steady}}$	=	Step response, K
$H_{\text{trans}}$	=	Impulse response, K
$h_v$	=	Volumetric heat transfer coefficient, $\text{W m}^{-3} \text{K}^{-1}$
$k$	=	Thermal conductivity, $\text{W m}^{-1} \text{K}^{-1}$
$K$	=	Parameter in Van Driest's model
$K_D$	=	Darcy coefficient, $\text{m}^2$
$K_F$	=	Forchheimer coefficient, m
$L$	=	Thickness, m
$m$	=	Mass, kg
$m^*$	=	Mass flow rate ratio $\dot{m}_c/\dot{m}_\infty$
$\dot{m}_A$	=	Mass flux, $\text{kg s}^{-1} \text{m}^{-2}$
$M$	=	Mach number
$n$	=	Exponent in viscosity law
$p$	=	Pressure, Pa
$\text{Pr}$	=	Prandtl number
$\text{Pr}_t$	=	Turbulent Prandtl number
$\dot{q}$	=	Heat flux, $\text{W m}^{-2}$
$r$	=	Recovery factor
$R$	=	Specific gas constant, $\text{J kg}^{-1} \text{K}^{-1}$
$R_N$	=	Nose radius, m
$\text{Re}$	=	Reynolds number
$s$	=	Length along the vehicle's surface, m
$s$	=	Reynolds analogy factor
$s'$	=	Transformed length along the vehicle's surface of Lee's model, m

$\tilde{s}$	=	Laplace-transformed time variable
$St$	=	Stanton number
$t$	=	Time, s
$T$	=	Temperature, K
$v$	=	Velocity, $\text{m s}^{-1}$
$W$	=	Length of porous injector, m
$x$	=	Spatial variable, m
$\alpha$	=	Cone half angle, rad
$\alpha$	=	Parameter in Van Driest's model
$\beta$	=	Parameter in Van Driest's model
$\delta$	=	Dirac impulse
$\eta$	=	Film effectiveness
$\epsilon$	=	Emissivity
$\kappa$	=	Isentropic coefficient
$\lambda$	=	Eigenvalue
$\mu$	=	Dynamic viscosity, Pa s
$\phi$	=	Porosity
$\rho$	=	Density, $\text{kg m}^{-3}$
$\rho_{pl}$	=	Reflectivity of the plenum
$\sigma$	=	Stefan-Boltzmann constant, $5.670367 \cdot 10^{-8} \text{ W m}^{-2} \text{ K}^{-4}$
$\theta$	=	Angle between flight direction and radius vector from center of curvature of nose, rad
$\xi$	=	Non-dimensional distance from injection point of Kutateladze's model
	=	

#### Subscripts

cone	=	On cone segment
crit	=	Critical
$f$	=	Coolant fluid
$g$	=	Hot gas, post shock
$i$	=	Iteration parameter
$j$	=	Iteration parameter
$n$	=	Iteration parameter
$pl$	=	Plenum

$r$	=	Recovery
ref	=	Reference
$s$	=	Solid
S-G	=	Sutton Graves
stag	=	Stagnation point
start	=	Initial value
steady	=	Steady state
trans	=	Transient
$\infty$	=	Free stream

#### Superscripts

$i$	=	At injection temperature
*	=	At temperature $T^*$

## I. Introduction

Re-entry of spacecraft or sustained hypersonic flight in the Earth's atmosphere leads to a high surface heat flux of the flight vehicles [1]. Thermal protection systems are used to keep wall temperatures below critical values, e. g. oxidation, sublimation or melting temperatures. Transpiration cooling is an active cooling technique that is envisaged for future hypersonic vehicles which experience high heat loads [2–8]. It relies on a gaseous or liquid fluid which is fed through a porous material [9–14]. The relatively cool fluid leads to convective cooling within the material and to the formation of a film that keeps the hot external gas further away from the surface and hence reduces the aerodynamic heat load significantly.

Although transpiration cooling was already recognised in the 1950s [15, 16], and a significant amount of research has been conducted since [11, 13, 17–21], very few vehicles have employed this technique. To date, only one hypersonic transpiration cooled flight experiment has been carried out, namely SHEFEX II [5]. The added complexity of an active system is a drawback that needs to be justified. Especially when the cooling technique is competing against proven technology, like ablative heat shields [22, 23]. However, transpiration cooling offers unique opportunities in the design of future hypersonic vehicles. The most noteworthy being re-usability of the entire thermal protection system and the associated efficiency since cooling can be activated only when required.

This paper details the methodology of the numerical approach and the respective validation thereof is presented. The existing body of literature has led to many engineering models that allow an estimation of the cooling performance for a given vehicle. A simulation tool has been developed that employs these models and allows for the efficient calculation of the material temperature of a porous wall for a given flight trajectory. The simulation is validated against a number of

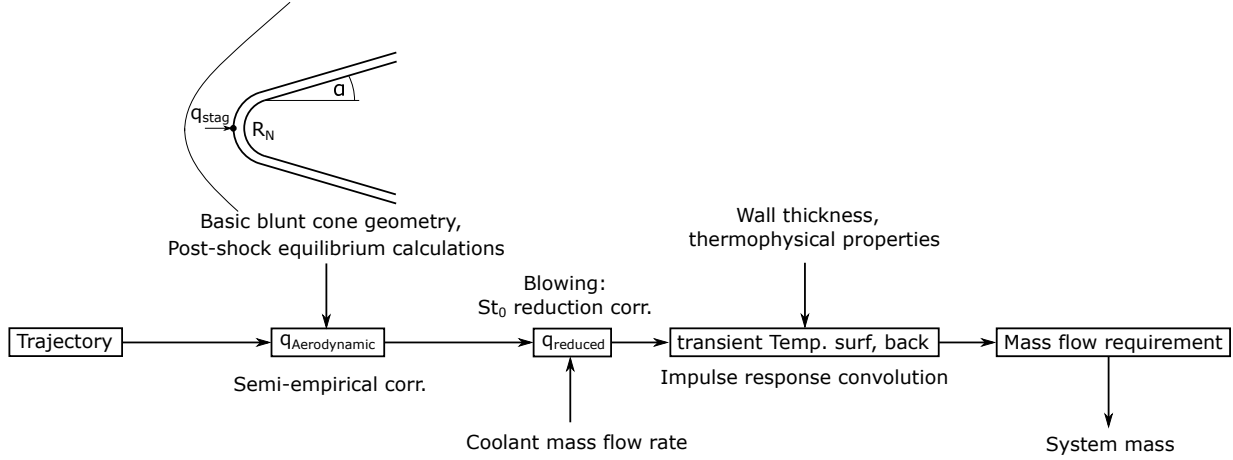


**Fig. 1 Flow chart of the computational approach.**

experimental studies performed in the plasma wind tunnel L2K and the SHEFEX II flight test.

## II. Model overview

The code *Porous Impulse Response Analysis for Transpiration cooling Evaluation* (PIRATE) developed for this investigation calculates the transient temperature response of a one dimensional porous transpiration cooled material that is subject to aerodynamic surface heating. Figure 1 presents an outline of the code. A majority of the model of this study has been based on the work of Böhrk et al. who developed a heat balance for porous materials and the associated external flow boundary layer (HEATS) [20]. In contrast to the work of Böhrk et al., the current model does not employ finite differences to solve the heat transfer in the material, but uses an approach based on impulse response convolution. The approach is used to optimise the spatio-temporal mass injection for transient calculations which is only practical for a quick calculation time. As the majority of the used correlations require various input parameters that are calculated at a later stage in the code, e. g. reservoir coolant density or wall temperature, the calculation is performed iteratively until convergence is obtained. The solution is considered converged when the change in calculated local mass flux is below 0.5 % compared to the previous iteration. The incentive for the layout of the code, i. e. mostly analytical or low-cost numerical schemes, is to apply the correlations from the large body of literature to assess the viability of transpiration cooling for a wide parameter space of hypersonic flight conditions. This requires a large amount of calculations to be performed and hence necessitates a quick convergence time for the numerical simulation. For the test-cases highlighted in section III the approach presented in this work requires approximately a factor of 200 less computational time compared to a classical finite element approach. This large gain in computational performance is mainly achieved through the analytical solution of the spatial domain in the material temperature, as will be detailed in section II.B.

## A. Aerodynamic heat flux

### 1. Aerodynamic correlations around vehicle

As a first step, a trajectory of a vehicle is chosen which is characterised by its velocity and altitude as a function of time. The aerodynamic heat flux is calculated for a specific entry capsule geometry. The common blunted cone geometry is used for investigations in this study where the stagnation point heat flux is determined using the correlation by Sutton and Graves with the hot wall correction [24]

$$\dot{q}_{S-G, \text{stag}} = 1.7415 \cdot 10^{-4} \cdot \left( \frac{\rho_{\infty}}{R_N} \right)^{0.5} \cdot v_{\infty}^3 \cdot \left( 1 - \frac{h_{\text{surface}}}{h_{\infty}} \right), \quad (1)$$

with the free stream density,  $\rho_{\infty}$ , the free stream velocity,  $v_{\infty}$ , the nose radius,  $R_N$ , and the wall and free stream enthalpies,  $h_{\text{surface}}$ , and,  $h_{\infty}$ . The heat flux along the body is determined using the correlation developed by Lees [25] which is detailed in the Appendix.

A number of post shock flow parameters are needed along the body length for subsequent calculations. Therefore, two *Chemical Equilibrium with Applications* (CEA) computations of the post shock flow state are conducted [26]. One simulation calculates the state after the normal shock on the stagnation streamline and one simulation determines the state after a conical shock which is calculated based on the cone angle of the vehicle [1]. It is assumed that the flow properties along the conical section are constant. The flow properties along the spherical surface are interpolated between stagnation point and conical section by applying the Newtonian flow solution, here presented for the case of static pressure,

$$p_g = p_{\text{stag}} + (p_{\text{cone}} - p_{\text{stag}}) \cdot \sin^2 \left( \frac{\theta}{\theta_{\text{crit}}} \frac{\pi}{2} \right), \quad \text{with } \theta = s/R_N \quad \text{and} \quad \theta_{\text{crit}} = \frac{\pi}{2} - \alpha. \quad (2)$$

with the length along the vehicle surface,  $s$ , and the cone half angle,  $\alpha$ . The CEA calculations are carried out for every time step of the considered trajectory, so that a spatially and temporally resolved post-shock state is determined. In the case of a flat plate geometry, van Driest's correlation for the aerodynamic heat flux is used which is detailed in the Appendix [27].

### 2. Film cooling

It is assumed that the entire simulated wall section of the vehicle consists of transpiration cooled porous material. However, it does not necessarily have to be actively cooled at every location along the vehicle surface. A sketch of the body model is shown in Fig. 2.

The length along the body,  $s$ , is discretised into different one-dimensional heat transfer problems. For the investigated case of a blunt body, the lateral heat flux between each segment is small and therefore neglected, i. e.  $\dot{q}_{\text{normal}} \gg \dot{q}_{\text{lateral}}$ .

The lateral heat fluxes encountered in the calculations performed are commonly two or more orders of magnitude lower than the heat flux component normal to the surface. The net heat flux to each segment of the vehicle wall is reduced by the formation of a coolant film. The film cooling is two part: The existing films of gas injection upstream of a certain segment contribute to a lower driving temperature, i. e. recovery temperature

$$T_{r,g} = T_{\infty} \left( 1 + r \frac{\kappa_g - 1}{2} M_g^2 \right), \quad r = \sqrt[2]{\text{Pr}_g} \quad (3)$$

based on the laminar correlation, with the Temperature,  $T$ , the Mach number,  $M$ , and the isentropic coefficient,  $\kappa$ , the Prandtl number,  $\text{Pr}$ , and parameters denoted by (g) referring to the hot post shock gas at the boundary layer edge [27]. The respective correlations for turbulent cases are detailed in the Appendix.

Additionally, the local bowing reduces the heat flux. By using the model of Kays et al. [28] for the local cooling and accounting for the different driving enthalpies in the respective Stanton numbers,  $\text{St}$ , the reduced heat flux is calculated by

$$\dot{q}_{\text{reduced}} = \dot{q}_{\text{S-G}} \frac{h_{r,\text{film}} - h_{\text{surface}}}{h_r - h_{\text{surface}}} \frac{B_h}{\exp(B_h) - 1}, \quad B_h = \frac{F}{\text{St}_{\text{uncooled}}} \left( \frac{c_{p,f}}{c_{p,g}} \right)^{0.6}, \quad (4)$$

with

$$F = \frac{\rho_f v_f}{\rho_g v_g}, \quad \text{St}_{\text{uncooled}} = \frac{\dot{q}_{\text{S-G}}}{\rho_g v_g (h_r - h_{\text{surface}})} \quad (5)$$

with coolant bulk velocity,  $v_f$ , specific heat capacity,  $c_p$ , enthalpy,  $h$ , and (f) denoting values of the coolant.

The film enthalpy is calculated by accounting for the temperature of the injected fluid,  $T_f$  (details on the determination of  $T_f$  are provided in section II.B), the locally absorbed heat flux, and the downstream film effectiveness which takes film-external flow mixing into account. When the coolant fluid is injected from the porous wall its state is dependent on

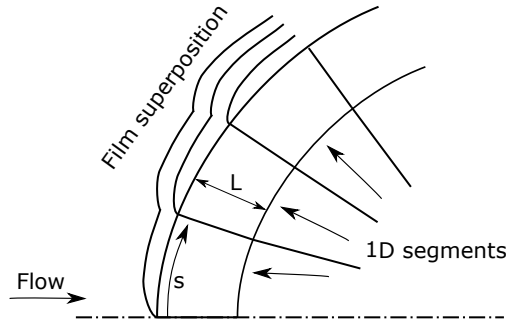


**Fig. 2 Schematic of the segmentation approach along the body.**

the temperature when it exits the porous material and on the absorption of part of the external aerodynamic heat flux,

$$T_{\text{injected coolant}} = \underbrace{T_f}_{\text{Temperature at injection}} + \underbrace{\frac{\dot{q}_{\text{S-G}} \left(1 - \frac{B_h}{\exp(B_h)-1}\right)}{c_{p,f} \rho_f V_f}}_{\text{Absorbed heat flux}}. \quad (6)$$

This slug of gas is then convected downstream and steadily mixes with the hot external flow which then decreases the film effectiveness [29],

$$\eta = \frac{T_{r,g} - T_{r,\text{film}}}{T_{r,g} - T_{\text{injected coolant}}}, \quad (7)$$

which is calculated using Kutateladze's model, as described in detail in the Appendix [18].

The superposition of different films from several injection points, as depicted in Fig. 2, is calculated using Seller's work [30]. The films are linearly superposed where the resulting film effectiveness of the downstream segment at spatial location  $s_i$  is determined via

$$T_{r,\text{film}}(s_i) = \eta(s_i) \cdot T_{\text{injected coolant}}(s_{i-1}) + (1 - \eta(s_i)) \cdot T_{r,\text{film}}(s_{i-1}) \quad (8)$$

with the convention

$$T_{r,\text{film}}(s_{i=0}) = T_{r,g}(s_i). \quad (9)$$

This formulation essentially states that each film forms a layer that mixes with the hot gas layer outside of it. However, in the case of a downstream location, the surrounding hot gas of the external flow has already mixed with the upstream films before and is hence cooled to a lower temperature. Equation (8) takes this effect into account. The so obtained film recovery temperature,  $T_{r,\text{film}}$ , is then used to evaluate the film recovery enthalpy,  $h_{r,\text{film}}$ , and Eq. (4) is used to calculate the resulting net heat flux for each location on the vehicle surface.

## B. Temperature in the porous material

The temperature of the solid and fluid phases within the vehicle wall is calculated, based on a given coolant mass flow rate, porous wall thickness and thermophysical properties of the solid and fluid phases. A semi-analytical approach is used utilising impulse or step responses of the porous material. The only temperatures calculated in the procedure are of the porous material surface and backside. The procedure does account for the entire temperature field within the material, but, in contrast to a finite element approach, does not calculate it at every point. In essence, this is what provides a much faster computation time. The thermal model used is one-dimensional and is therefore only suitable for cases where the lateral heat flux is negligible when compared to the normal heat transfer, i. e.  $\dot{q}_{\text{normal}} \gg \dot{q}_{\text{lateral}}$ . In the following, the boundary conditions of the thermal model and the calculation methodology are presented. A schematic



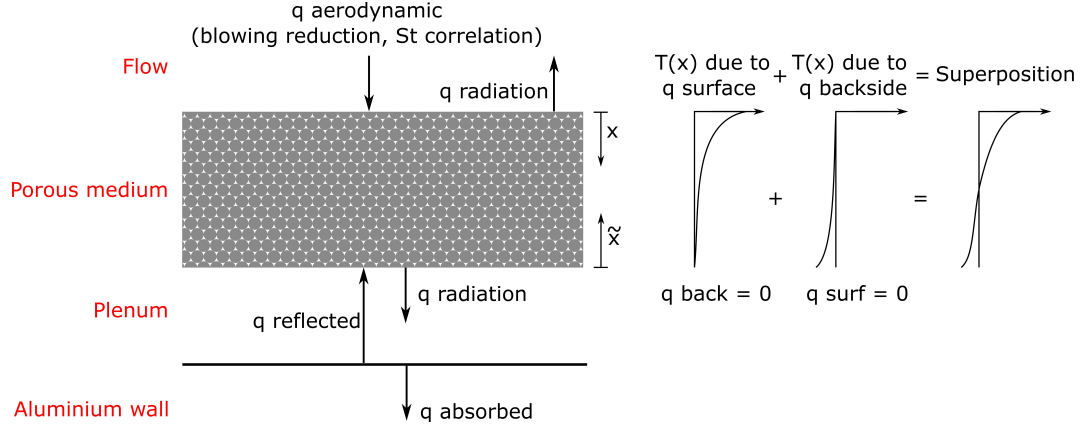


**Fig. 3 Schematic of the one-dimensional thermal model.**

overview of the wall model is shown in Fig. 3.

The net surface heat flux is calculated based on the cooled aerodynamic heat flux and also accounts for radiative cooling via

$$\dot{q}_{\text{surface}} = \dot{q}_{\text{reduced}} - \sigma \epsilon_s T_{\text{surface}}^4 \quad (10)$$

with the Stefan-Boltzmann constant,  $\sigma$ , and the surface emissivity,  $\epsilon_s$ . It is assumed that an aluminium plenum is located behind the porous material. Between the plenum surface and the backside of the porous wall, heat transfer in form of radiation can occur. This leads to a negative net backside heat flux that is calculated from the balance of the radiative heat exchange terms,

$$\dot{q}_{\text{backside}} = - \frac{\sigma (T_{\text{backside}}^4 - T_{pl}^4)}{\frac{1}{\epsilon_s} + \frac{1}{\epsilon_{pl}} - 1} \quad (11)$$

with the aluminium plenum emissivity  $\epsilon_{pl} = 0.07$  and the respective temperature  $T_{pl}$  which is assumed to be at ambient conditions. Through the variation of the plenum temperature and reflectivity, different rear boundary conditions can be set, e. g. a fully adiabatic backside for  $\epsilon_{pl} = 0$ . In the following, the derivation of the step and impulse responses of porous media are presented. Thereafter, their application in the current model is discussed.

### 1. Derivation of step and impulse responses

The governing equations are the energy equations for solid and fluid phase are [31]

$$(1 - \phi) \rho_s c_{p,s} \frac{\partial T_s}{\partial t} = k_s (1 - \phi) \frac{\partial^2 T_s}{\partial x^2} + h_v (T_f - T_s) \quad (12)$$

and

$$\phi \rho_f c_{p,f} \frac{\partial T_f}{\partial t} = \phi \rho_f c_{p,f} \frac{v_f}{\phi} \frac{\partial T_f}{\partial x} + h_v (T_s - T_f), \quad (13)$$

with (s) denoting the solid phase, (f) denoting the fluid phase, the thermal conductivity,  $k$ , the porosity,  $\phi$ , the volumetric heat transfer coefficient,  $h_v$ , the time,  $t$ , and the location,  $x$ , measured from the surface. Note that the convention used in these equations is a temperature difference to the initial starting temperature,  $T_{\text{start}}$ . The equations are solved for the boundary conditions of a constant fluid temperature at the plenum side with material thickness,  $L$ ,

$$x = L, \quad T_f = 0, \quad (14)$$

an adiabatic backside

$$x = L, \quad \frac{\partial T_s}{\partial x} = 0, \quad (15)$$

and a unit surface heat flux

$$x = 0, \quad \dot{q} = -(1 - \phi) k_s \frac{\partial T_s}{\partial x} = 1 \text{ Wm}^{-2}. \quad (16)$$

for steady state calculations or a Dirac impulse

$$x = 0, \quad \dot{q}(t) = -(1 - \phi) k_s \frac{\partial T_s(t)}{\partial x} = \delta(t = 0), \quad \text{where} \quad \int_0^\infty \dot{q}(t) dt = 1 \text{ Jm}^{-2} \quad (17)$$

for transient calculations.

In the case of a steady state, i. e. a time derivative of zero in Eqs. (12) and (13), the employed approach is similar to the work of Schweikert et al. [32]. The calculation results in the steady state temperature (i. e. the step response at a time of infinity) for a continuous unit surface heat flux of

$$H_{s, \text{steady}} = \sum_{i=1}^3 C_i \exp(\lambda_i x) \quad (18)$$

for the solid phase and

$$H_{f, \text{steady}} = \sum_{i=1}^3 C_i \left( 1 - \lambda_i^2 \frac{k_s(1 - \phi)}{h_v} \right) \exp(\lambda_i x) \quad (19)$$

for the fluid phase with the Eigenvalues

$$\lambda_{1,2} = \frac{h_v}{2\rho_f c_{p,f} v_f} \pm \sqrt{\left( \frac{h_v}{2\rho_f c_{p,f} v_f} \right)^2 + \frac{h_v}{k_s(1 - \phi)}}, \quad \text{and} \quad \lambda_3 = 0. \quad (20)$$

The coefficients  $C_i$  are obtained from solving the linear system of equations

$$\begin{pmatrix} B_1 \exp(\lambda_1 L) & B_2 \exp(\lambda_2 L) & 1 \\ \lambda_1 \exp(\lambda_1 L) & \lambda_2 \exp(\lambda_2 L) & 1 \\ \lambda_1 & \lambda_2 & 1 \end{pmatrix} \cdot \begin{pmatrix} C_1 \\ C_2 \\ C_3 \end{pmatrix} = \begin{pmatrix} 0 \\ 0 \\ \frac{-1}{k_s(1-\phi)} \end{pmatrix} \quad (21)$$

with

$$B_{1,2} = 1 - \lambda_{1,2}^2 \frac{k_s(1-\phi)}{h_v}. \quad (22)$$

Equations (21) and (22) are a representation of the boundary conditions (14)-(16) in the Laplace space.

For transient calculations, impulse responses of both solid and fluid phases are required. They are calculated analytically in the Laplace-space (variable  $\tilde{s}$ ) after transforming the time domain (variable  $t$ ) of Eqs. (12) and (13). The solid impulse response, i. e. the temperature evolution after the exposure to a unit Dirac impulse of surface heat flux, is determined to be

$$H_{s, \text{trans}} = \sum_{i=1}^3 C_i \exp(\lambda_i x) \quad (23)$$

and the fluid impulse response is calculated by

$$H_{f, \text{trans}} = \sum_{i=1}^3 C_i \left( \frac{\tilde{s}(1-\phi)\rho_s c_{p,s}}{h_v} + \frac{k_s(1-\phi)}{h_v} \lambda_i^2 \right) \exp(\lambda_i x). \quad (24)$$

The eigenvalues,  $\lambda_i$ , are calculated by solving the characteristic equation

$$A_3 \lambda_{1-3}^3 + A_2 \lambda_{1-3}^2 + A_1 \lambda_{1-3} + A_0 = 0. \quad (25)$$

with the coefficients

$$A_0 = \frac{h_v}{(1-\phi)\rho_s c_{p,s}} \frac{h_v}{\phi \rho_f c_{p,f}} - \left( \tilde{s} + \frac{h_v}{(1-\phi)\rho_s c_{p,s}} \right) \left( \tilde{s} + \frac{h_v}{\phi \rho_f c_{p,f}} \right), \quad (26)$$

$$A_1 = \frac{v_f}{\phi} \left( \tilde{s} + \frac{h_v}{(1-\phi)\rho_s c_{p,s}} \right), \quad (27)$$

$$A_2 = \frac{k_s}{\rho_s c_{p,s}} \left( \tilde{s} + \frac{h_v}{\phi \rho_f c_{p,f}} \right), \quad (28)$$

$$A_3 = -\frac{v_f}{\phi} \frac{k_s}{\rho_s c_{p,s}}. \quad (29)$$

The coefficients  $C_i$  are again a function of the boundary conditions (14), (15) and (17) in the Laplace space and are

determined from solving the linear system of equations

$$\begin{pmatrix} B_1 \exp(\lambda_1 L) & B_2 \exp(\lambda_2 L) & B_3 \exp(\lambda_3 L) \\ \lambda_1 \exp(\lambda_1 L) & \lambda_2 \exp(\lambda_2 L) & \lambda_3 \exp(\lambda_3 L) \\ \lambda_1 & \lambda_2 & \lambda_3 \end{pmatrix} \cdot \begin{pmatrix} C_1 \\ C_2 \\ C_3 \end{pmatrix} = \begin{pmatrix} 0 \\ 0 \\ \frac{-1}{k_s(1-\phi)} \end{pmatrix} \quad (30)$$

with

$$B_i = \frac{\bar{s}(1-\phi)\rho_s c_{p,s}}{h_v} + \frac{k_s(1-\phi)}{h_v} \lambda_i^2. \quad (31)$$

The so determined analytical solution in the Laplace space is transformed back to the time domain by using the algorithm of Gaver and Stehfest [33, 34]. Further details of the derivation of these porous medium impulse responses are presented in detail in Ref. [35].

Additionally, the transient change in plenum coolant temperature is considered that can lead to a further source of heating of the porous material, an effect that was present in some of the validation cases (presented in section III). To account for this phenomenon the same methodology is used as described above. However, the boundary conditions are changed appropriately to a Dirac impulse of coolant temperature,

$$x = L, \quad T_f = \delta(t = 0), \quad \text{where} \quad \int_0^\infty T_f(t) dt = 1 \text{ Ks}, \quad (32)$$

an adiabatic backside

$$x = L, \quad \frac{\partial T_s}{\partial x} = 0, \quad (33)$$

and an adiabatic surface

$$x = 0, \quad \frac{\partial T_s}{\partial x} = 0. \quad (34)$$

This results in the alteration to (1 0 0) of the right hand side of Eq. (30). The obtained impulse response of the solid material is labelled as  $H_{s, \text{trans}, T}$  and describes the solid temperature evolution at a given depth after a unit temperature impulse of the plenum coolant.

## 2. Steady state temperature calculation

This section describes how the step responses are used to calculate the surface and backside temperatures of the porous material. As the used differential equation system, Eqs. (12) and (13), is linear, it is possible to superpose different solutions and thus account for a non-adiabatic backside or for the change in plenum coolant temperature. As depicted in Fig. 3, the different heating sources are used to calculate the respective temperature fields in the material. Every heating source, e. g. surface or backside heat flux, leads to a temperature change. All the temperature changes are

then superposed to obtain the combined temperature field. As the heat flux terms also depend on these temperature fields, an iterative approach is used to calculate the heat flux boundary conditions and the temperature fields until convergence is obtained.

For steady state cases (no transient change in plenum coolant temperature is considered here), the solid temperatures at the surface and backside are calculated via

$$T_{s,\text{surface}} = H_{s,\text{steady}}(x = 0) \cdot \dot{q}_{\text{surface}} + H_{s,\text{steady}}(x = L) \cdot \dot{q}_{\text{backside}} + T_{\text{start}} \quad (35)$$

and

$$T_{s,\text{backside}} = H_{s,\text{steady}}(x = L) \cdot \dot{q}_{\text{surface}} + H_{s,\text{steady}}(x = 0) \cdot \dot{q}_{\text{backside}} + T_{\text{start}}. \quad (36)$$

The surface fluid temperature is determined by

$$T_f = H_{f,\text{steady}}(x = 0) \cdot \dot{q}_{\text{surface}} + T_{\text{start}}, \quad (37)$$

with the initial temperature  $T_{\text{start}}$ .

### 3. Transient temperature calculation

The transient calculations are based on the impulse response principle [36]. The same linear superposition approach is used as described in section II.B.2. The solid material temperatures at the surface and backside are determined via the discrete convolutions

$$T_{s,\text{surface}}(t_i) = \sum_{t_j=t_0}^{t_i} H_{s,\text{trans}}(t_j, t_{i-j}, x = 0) \cdot \dot{q}_{\text{surface}}(t_j) + \sum_{t_j=t_0}^{t_i} H_{s,\text{trans}}(t_j, t_{i-j}, x = L) \cdot \dot{q}_{\text{backside}}(t_j) + \sum_{t_j=t_0}^{t_i} H_{s,\text{trans},T}(t_j, t_{i-j}, x = 0) \cdot T_{f,pl}(t_j) + T_{\text{start}} \quad (38)$$

and

$$T_{s,\text{backside}}(t_i) = \sum_{t_j=t_0}^{t_i} H_{s,\text{trans}}(t_j, t_{i-j}, x = L) \cdot \dot{q}_{\text{surface}}(t_j) + \sum_{t_j=t_0}^{t_i} H_{s,\text{trans}}(t_j, t_{i-j}, x = 0) \cdot \dot{q}_{\text{backside}}(t_j) + \sum_{t_j=t_0}^{t_i} H_{s,\text{trans},T}(t_j, t_{i-j}, x = L) \cdot T_{f,pl}(t_j) + T_{\text{start}}. \quad (39)$$

The surface fluid temperature is calculated by

$$T_f(t_i) = \sum_{t_j=t_0}^{t_i} H_{f,\text{trans}}(t_j, t_{i-j}, x = 0) \cdot \dot{q}_{\text{surface}}(t_j) + T_{f,pl}(t_i) + T_{\text{start}}. \quad (40)$$

The inclusion of a time-varying coolant mass flux results in a change of the impulse response over time. The change in the thermal properties of the porous medium is approximated by combining different impulse responses which correspond to different coolant mass fluxes,  $\dot{m}_A$ . This strategy has been employed for inverse heat transfer investigations in the past, where time-varying impulse responses are considered [37, 38]. It is usually referred to as the sequential function specification method [39] and the details of the approach are given in the following. An impulse response  $H_{s,f \text{ trans}}(t_j, t_i, x) = f(v_f(t_j))$  is calculated for each time step,

where  $t_j$  is the starting time of the impulse response and  $t_i$  is the temperature evolution of this particular impulse response. However, the changing coolant velocity of the following time steps will also affect the evolution of the impulse response. This is approximated by changing the normalised gradient of the impulse response  $H_{s,f \text{ trans}}(t_j, t_{i-j}, x)$  to be equal to the normalised gradient of the impulse response  $H_{s,f \text{ trans}}(t_i, t_{i-j}, x)$  and thus accounting for the change in coolant velocity with time:

$$H_{s,f \text{ trans}}(t_j, t_{i-j}, x) = H_{s,f \text{ trans}}(t_j, t_{i-j-1}, x) \left( 1 + \frac{H_{s,f \text{ trans}}(t_i, t_{i-j}, x) - H_{s,f \text{ trans}}(t_i, t_{i-j-1}, x)}{H_{s,f \text{ trans}}(t_i, t_{i-j-1}, x)} \right), \quad (41)$$

for  $t_i > t_j$  and  $t_0 < t_j < t_{\text{end}}$ .

### C. Reservoir pressure

The calculated fluid temperatures in the material will have an effect on the plenum pressure  $p_{pl}$  since a higher coolant temperature leads to a higher viscosity in the material and this will therefore lead to a higher required plenum pressure for a given mass flux. The governing equation of this process is the Darcy-Forchheimer equation,

$$-\frac{\partial p}{\partial x} = \frac{\mu_f}{K_D} v_f + \frac{\rho_f}{K_F} v_f^2, \quad (42)$$

with pressure,  $p$ , coolant dynamic viscosity,  $\mu_f$ , Darcy-coefficient,  $K_D$ , and Forchheimer coefficient,  $K_F$ . Analogous to Langener [9], a simplified linear solution of the temperature field in the medium can be used to solve the Darcy-Forchheimer equation analytically to

$$p_{pl} = \sqrt{p_g^2 + \frac{2L}{T_f - T_{s,\text{backside}}} \left[ \frac{\dot{m}_A R \mu_{f,\text{ref}}}{(n+2) K_D T_{\text{ref}}^n} (T_f^{n+2} - T_{s,\text{backside}}^{n+2}) + \frac{\dot{m}_A^2 R}{2K_F} (T_f^2 - T_{s,\text{backside}}^2) \right]} \quad (43)$$

with the viscosity law exponent,  $n = 0.69$ , the specific gas constant,  $R$ , and the viscosity reference temperature,  $T_{\text{ref}}$  [9]. The coolant density is then obtained by using the ideal gas law and is used to update the impulse responses. The described procedure is conducted for every segment along the vehicle surface.

### III. Validation test cases

Several Validation cases are considered where the results obtained with the numerical model are compared to experimental data, the heat balance finite difference solver HEATS, and the finite volume Navier-Stokes code LAURA. In particular, experimental results from the SHEFEX II flight test campaign, and the RESPACE and IMENS+ campaigns are used [5, 6]. SHEFEX II is the only transpiration cooled flight data available in open literature and thus provides a very valuable dataset to validate numerical models. In addition, the plasma wind tunnel test campaign provides experimental data at high enthalpy conditions, as expected during re-entry, which is the main focus of the present work. The material parameters of the porous injectors used in the investigated experiments are summarised in Table 1. Please note that these values are measured effective material properties, i. e. where the porosity has already been taken into account. The parameters given in Table 1 therefore refer to the effective thermal conductivity  $(1 - \phi)k_s$  and to the effective density  $(1 - \phi)\rho_s$ . The volumetric heat transfer coefficient is estimated to be  $1 \cdot 10^4 \text{ W m}^{-3} \text{ K}^{-1}$  based on the work of Florio et al. [40].

#### A. Flat plate plasma wind tunnel experiments - uncooled

Experiments are considered which have been conducted in the DLR wind tunnel L2K during the RESPACE and IMENS+ test campaigns. The experimental setup is a flat plate (see Fig. 4) with a blunted nose which was oriented at an angle of attack of  $20^\circ$  to the supersonic plasma flow. Porous injectors are mounted on the surface of the plate and transient surface temperature traces have been recorded using infra red thermography at various locations on the model as depicted in Fig. 5.

The inflow conditions of the plasma wind tunnel and the measurement location downstream of the leading edge are taken from Ref. [6] and summarised in Table 2. The resulting Reynolds number is on the order of  $10^4$  which means that the flow can be assumed to be laminar. In addition, it is assumed that any entropy layer is smaller than the boundary layer. Therefore, oblique shock relations are used to approximate the conditions at the boundary layer edge. The measured free stream species composition, as reported in Ref. [6], is used to calculate the free stream isentropic

**Table 1 Sample properties for the experimental tests [6, 20].**

Parameter	C/C standard	C/C-SiC
$\phi$	0.13	-
$\rho_s / \text{kg m}^{-3}$	1400	1900
$\epsilon_s$	0.88	0.88
$k_s / \text{W m}^{-1} \text{ K}^{-1}$	2	8.4
$c_{p,s} / \text{J kg}^{-1} \text{ K}^{-1}$	1650	1350
$K_D / \text{m}$	$1.645 \cdot 10^{-13}$	-
$K_F / \text{m}^2$	$2.9 \cdot 10^{-6}$	-
$h_v / \text{W m}^{-3} \text{ K}^{-1}$	$1 \cdot 10^4$	-



**Fig. 4** Model used in L2K screening test [6].  
1) KAPYROX insulation, 2) frame structure,  
3) cover plate, 4) porous sample.

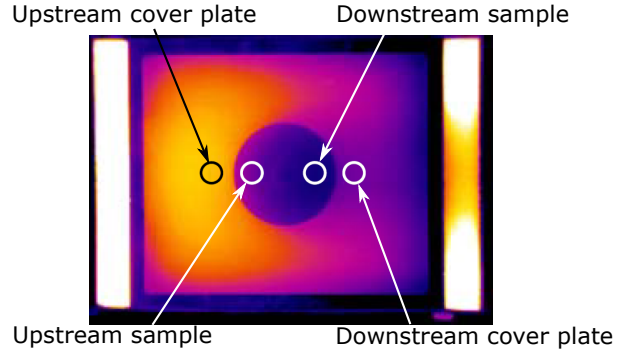


**Fig. 5** Infrared thermography image of L2K experiments [6].

**Table 2** Flow conditions for the plasma wind-tunnel experiments.

Condition	L2K
M	7.0
$p_{\infty}$ , Pa	47
$T_{\infty}$ , K	378
Total enthalpy, MJ/kg	8.4

coefficient which is subsequently employed in the oblique shock relations. The post shock conditions are estimated by assuming thermochemical equilibrium and the NASA *Chemical Equilibrium with Applications* (CEA) model is used to calculate the post shock conditions. The Prandtl number is assumed to be 0.75 and Sutherland's law is used to calculate the viscosity. The stagnation point of the model is chosen as the origin of body coordinate  $s$ . The surface heat flux is determined by applying the method of Van Driest [27].

The thermal model using a 6 mm thick C/C-SiC material with an adiabatic backside, and a time discretisation of 0.15 s is compared to the measured surface temperatures at a location on the cover plate upstream of the porous sample denoted as *upstream sample* in Fig. 5. For the first of the considered cases, a PIRATE simulation using C/C-SiC material data is compared to the measured surface temperatures at a location on the cover plate upstream of the porous sample. The investigated location is at a distance of 135 mm from the leading edge stagnation point. As shown in Fig. 6, the numerical simulations match well with the experimental traces. The final temperature of the simulation lies within 40 K of the experimental value and deviates up to 10% of the absolute measured temperature during the heating phase, providing a minor overestimate compared to the result of the HEATS finite difference code. The differences in final temperature can be attributed to two factors. First of all, PIRATE only considers normal heat transfer through the material and neglects lateral conduction. This explains the difference in the shape of the temperature rise compared to HEATS which includes lateral conduction where heat can diffuse from the hotter upstream section to the measurement



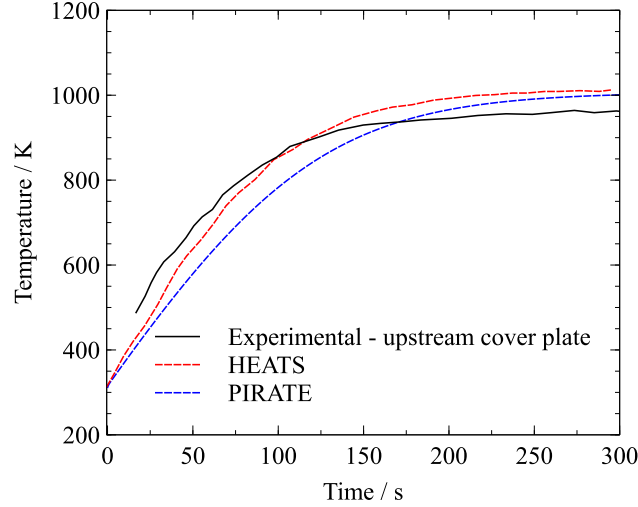


**Fig. 6 Comparison of simulation results to measured surface temperature at AoA = 20 degrees in L2K [6].**

area. In addition, the simulation assumes an adiabatic back wall condition similar to HEATS. In reality, there will be some limited conduction at the back wall which explains the slightly reduced final temperature reached in the experiment. This comparison confirms that the thermal modelling leads to a good agreement with experimental data for uncooled cases. Additional effects including cooling through gas injection are considered in the following case.

### **B. Flat plate plasma wind tunnel experiments - transient transpiration cooling**

In this case of the validation study, transpiration cooled porous materials are investigated. The same experimental campaign described in section III.A (RESPACE and IMENS+ [6]) investigates the effectiveness of transpiration cooling for various coolant mass flow rates of Nitrogen. In the study, continuous plasma wind tunnel free stream conditions are maintained while the coolant mass flow rate is varied in steps over the test time of the experiment. IR thermography was used to determine the transient surface temperature of the porous sample, denoted as *downstream sample* in Fig. 5. By applying the same free stream conditions as presented in Table 2, the transient wall temperatures with the coolant gas are simulated.

Figure 7 shows the variation in mass flow rate and the measured transient surface temperature. The experiment used a C/C standard porous material located approximately 200 mm from the model stagnation point. In the PIRATE simulation of the experiment the coolant temperature in the plenum is increasing to a maximum of 422 K which was also measured in the experiment. The linear rise and fairly constant plateau at later times is representative of a typical test condition as presented in Ref. [6]. The C/C-SiC plenum behind the porous sample is modelled by accounting for the respective radiation loss at the backside. This is taken into account by using a radiative back boundary condition as described in section II.B. Additionally, the results obtained by a HEATS simulation of this experiment are included. At short times both simulations and the experimental data agree well whereas at long times, the PIRATE simulation

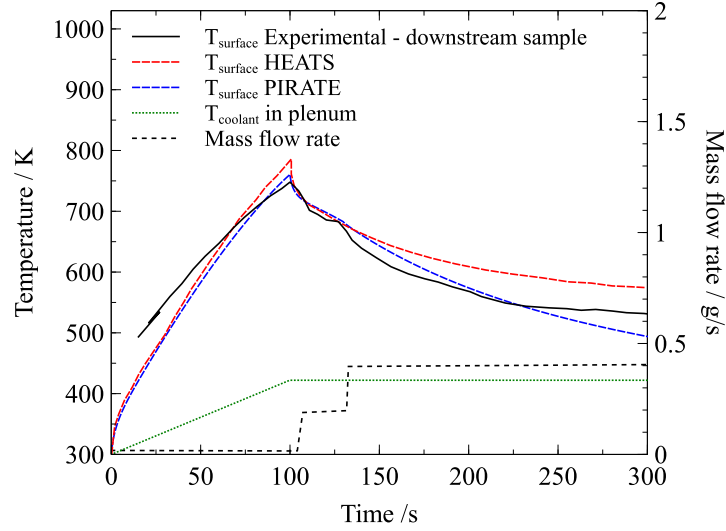


**Fig. 7 Comparison between PIRATE, HEATS and experimental measurements of a C/C sample [6, 20].**

slightly under predicts the porous sample surface temperature and the respective HEATS simulation results in an over prediction. As the HEATS simulation used an adiabatic backside condition, the higher predicted temperature seems reasonable. The additional radiative losses at the plenum side result in a lower temperature for the PIRATE simulation. A reason for the higher measured surface temperature at approximately 300 s could be the result of an increase in the temperature of the structure below the cooled surface. The overall agreement between the PIRATE simulation and the experimental data is very good. Hence, transient transpiration cooling effects at the injection location are sufficiently captured by the model approach.

### C. Hemisphere - transpiration cooled

This case is used to investigate heat transfer to a transpiration cooled hemispherical model. The experiments are reported in Ref. [41] and have also been used in Ref. [42] to validate the finite-volume Navier-Stokes code LAURA. The experiments were carried out with the porous hemispherical model shown in Fig. 8. The model consisted of a porous stainless steel wall with a pressure chamber behind that fed the coolant (air) to the surface. The injected mass flux distribution along the model circumference was measured and used as a direct input for PIRATE. The heat flux was measured using thermocouple copper calorimeter gauges. The flow around the model featured a total pressure of 52.2 bar, a total temperature of 761 K, a unit Reynolds number of  $12.9 \cdot 10^6 \text{ m}^{-1}$ , and a Mach number of 7.32. These inflow conditions were used to deduce the free stream quantities needed for a PIRATE simulation which has been carried out for no injection, and the experimentally measured mass flow rate ratio  $m^* = 0.004$ . The investigated flow remained laminar along the surface of the hemisphere. No other reported transitional conditions of Ref. [41] are considered as no assumption about a transitional Reynolds number criterion with mass injection was made.

The simulated surface heat flux is compared to the experimental measurements in Fig. 9 which also includes the

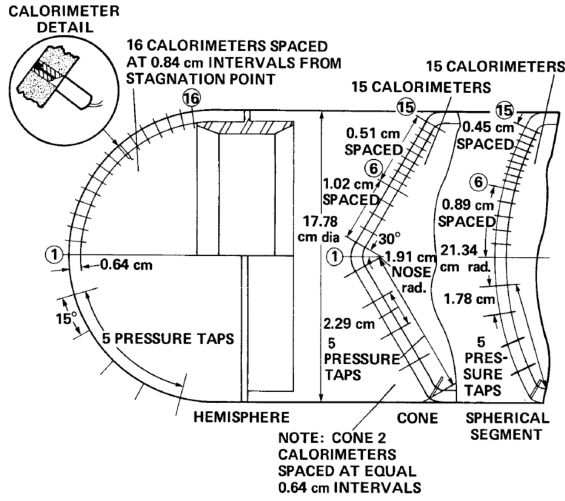


**Fig. 8** Porous hemisphere model used in Ref. [41].

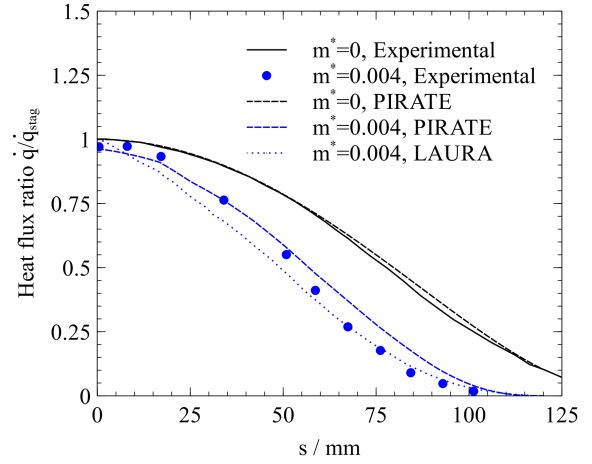


**Fig. 9** Measured, PIRATE simulated, and LAURA simulated heat flux with and without mass injection [41, 42].

LAURA simulation result. Both the PIRATE and LAURA results agree very well with the experimental measurements. This example highlights that the blunt body heat transfer correlations used in PIRATE produce satisfactory results, similar to a CFD code, and it also highlights the applicability of the coolant injection model for a curved body.

#### D. SHEFEX II - uncooled

The fourth validation test case aims to investigate the temperature change when the vehicle is exposed to a transient heat flux. The published flight data of the sharp edge flight experiment SHEFEX II (see Fig. 10) was used to address this case [5]. The total flight time was roughly 500 s with 52 s of experimental time for the atmospheric re-entry at altitudes between 100 and 30 km. SHEFEX II re-entry data at Panels B and D are simulated with a time discretisation of 0.1 s and compared with the respective experimental data (with 3 mm thick C/C-SiC material properties). The entire trajectory from launch to the end of the experiment is simulated and the DMARS altitude and velocity data have been used to assess the free stream conditions [5]. Due to the tilted nose panels of the vehicle, an oblique shock is formed and oblique shock relations are used to determine the post shock state variables. The SHEFEX II heat shield changes to other angles in the subsequent segments B, C, D and E downstream of the nose tip (see Fig. 10). The flow conditions on these panels downstream of the leading edge are all calculated by Prandtl-Meyer expansion theory [20]. The respective surface heat flux is calculated by applying the method of Van Driest [27].

Fig 11 shows thermocouple measurements located 1 mm below the surface at panels B and D (at  $x = 303$  mm and  $x = 913$  mm from the stagnation point, see Fig. 10), averaged over four instrumented circumferential panels over the re-entry flight time. The simulation was undertaken at all three thermocouple locations and also compared to the respective transient temperature predictions of HEATS. The in-depth temperatures are probed by using the form of Eqs. (38)

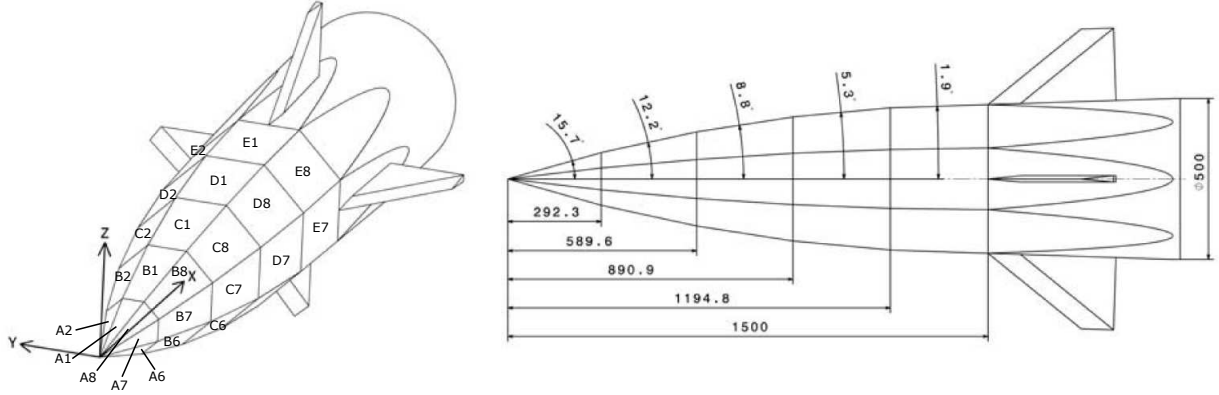


**Fig. 10** Coordinate system and dimensions of the SHEFEX II forebody [43]

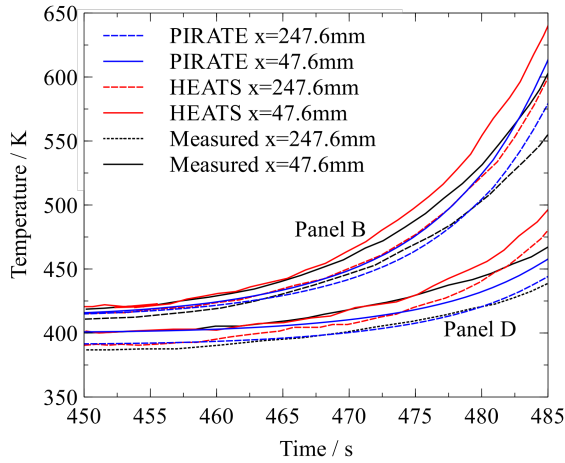


**Fig. 11** Comparison of simulation results to SHEFEX II measurements at panels B and D (see Fig. 10 for axial distance  $x$ ) [5].

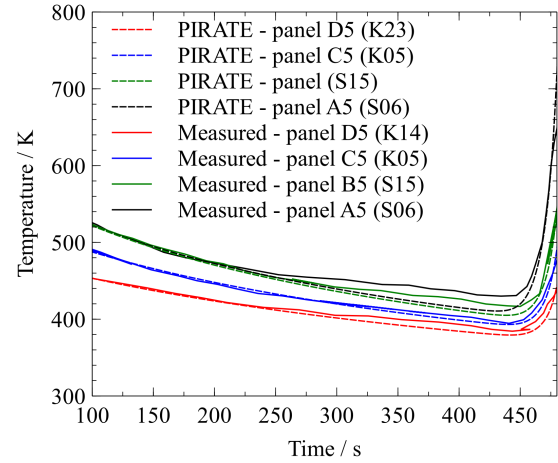


**Fig. 12** Measured vs PIRATE simulation temperatures at row 5.

and (39) for a location  $b = 1$  mm within the material,

$$T_{s,b}(t_i) = \sum_{t_j=t_0}^{t_i} H_{s \text{ trans}}(t_j, t_{i-j}, x = b) \cdot \dot{q}_{\text{surface}}(t_j) + \sum_{t_j=t_0}^{t_i} H_{s \text{ trans}}(t_j, t_{i-j}, x = L - b) \cdot \dot{q}_{\text{backside}}(t_j) + T_{\text{start}}. \quad (44)$$

As Fig. 11 shows, both HEATS and PIRATE simulations match very well. The measurements are systematically below the simulated temperatures. This may be attributed to adiabatic back side assumption made by both HEATS and PIRATE, whereas the real material will experience heat conduction away to the substructure during flight.

In addition, from  $t=100$  s to  $t=480$  s the measured temperatures at the foremost thermocouple position along panel row 5 have been compared to PIRATE simulations in Fig. 12. Again, the un-cooled case agrees with the thermocouple

results to within 5 %, based on the absolute measured temperature, with maximum deviations of 30 K. This suggests that that PIRATE simulations is a valid tool to predict transient temperature distributions along a vehicle over an entire flight trajectory.

#### **E. SHEFEX II - transpiration cooled downstream film**

The final validation case aims to investigate transient temperature reduction due to the film effect downstream of a coolant injection through a porous sample. The SHEFEX II flight experiment implemented a ceramic based transpiration-cooled experiment named AKTiV. Porous C/C samples (properties from Table 1) with a thickness of 5 mm were inserted in the centre of a 7 mm thick thermal protection panel. The coolant gas is Nitrogen which is fed through the porous sample and the reservoir is made of stainless steel. Figure 13 shows the locations of thermocouples for the AKTiV experiment.

Results from the PIRATE simulations are compared with the thermocouple (located 1 mm below the surface) measurements upstream and downstream of the sample at three different locations in Fig. 14. The spatial distribution of the measured and simulated temperatures is shown in Fig. 15 for the time  $t = 485$  s. The reservoir coolant temperature was taken as 300 K [5]. Before the cooling is started at 431 s, the pre-heating of the model has been simulated by using the measured material temperature as the starting value. The prediction of the temperature reduction due to cooling is in good accordance with both HEATS and the experiment and lies within a margin of less than 5% of the absolute measured temperature during the trajectory with maximum deviations of 20 K. There is a slightly different trend in the cooling between HEATS and PIRATE simulations. This may be attributed to the different models used between HEATS and PIRATE to calculate the downstream film effectiveness. Where HEATS uses a boundary layer heat balance, PIRATE uses a semi-empirical correlation.

In conclusion, the different validation cases have demonstrated that results from the numerical model developed match experimental data closely and can therefore be used as a tool to investigate the effect of transpiration cooling for Earth re-entry on a system study level. A similar degree of agreement has been reported by Böhrk et al. [20] for HEATS, which is of comparable numerical sophistication as the current work. The relevant effects occurring during transpiration cooled hypersonic flight, i. e. transient heating, local cooling through blowing, and downstream film coverage, are replicated well.

## **IV. Conclusion**

This paper presents a numerical model that has been developed to perform rapid simulations of the transient temperature evolution of transpiration cooled heat shields for hypersonic vehicles. Correlations from the open literature are used to assess the aerodynamic heat flux along the vehicle. Local Stanton number reduction and downstream film cooling are taken into account. A one-dimensional impulse response convolution approach is used to determine the

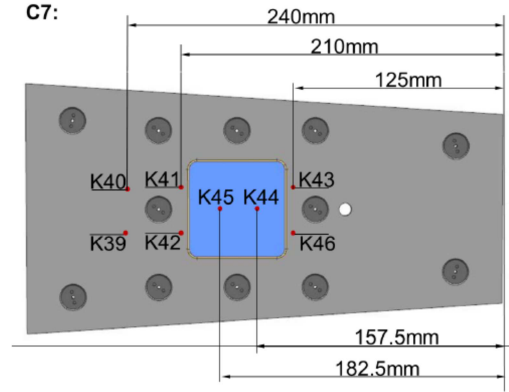


**Fig. 13** AKTiV thermocouple locations on experiment [5].

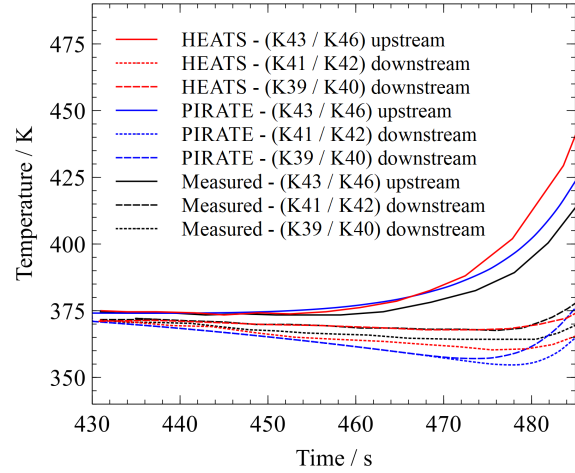


**Fig. 14** Measured and simulated material temperature during flight upstream and downstream of porous sample [5].

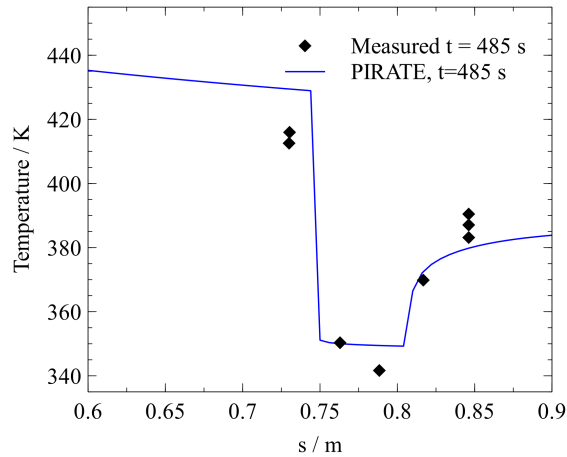


**Fig. 15** Spatial distribution of measured and simulated temperatures around the porous injector for  $t = 485$  s [5].

transient or steady state temperature of the porous material of the heat shield. The employed impulse response approach approximates the material temperature using a simplification of the heat conduction problem, e. g. the omission of lateral heat conduction and the transient change of impulse responses. However, it also leads to a significant reduction of the required computation time compared to a classical finite element approach. Depending on the test case, this can be as high as two orders of magnitude.

The model is validated using data of experiments in the L2K plasma wind tunnel and data from the SHEFEX II re-entry flight test. Experiments in the L2K wind tunnel show good agreement between experiment and simulation for solid un-cooled C/C-SiC and porous transpiration cooled C/C. The temperature trend due to the transient change in coolant mass flux is replicated well by the simulation, showing good performance of the local cooling and material model. The comparison between experiment and simulation of un-cooled SHEFEX II wall temperatures also showed good agreement which demonstrates that highly transient flow conditions can be simulated. Finally, the good agreement of wall temperatures downstream of the injection point of the porous C/C injector on SHEFEX II shows that the downstream film effect including flow-film mixing is sufficiently resolved. Overall, the agreement between experiment and simulation is good and material temperature deviations are smaller than 10 % at all times. For the studied cases, the highest deviation from the experimental values was found to be 40 K. Furthermore, a good agreement between HEATS and PIRATE is found for all validation studies, which shows that the different numerical approaches in the current work lead to a similar result.

The developed model is thus suited for systematic studies of transpiration cooled flight vehicles. A large number of computations can be performed in a relatively short time, which allows for optimisation studies and the systematic investigation of the hypersonic parameter space.

## Appendix

### Lee's model for the heat flux distribution around a blunt body

The heat flux distribution along the vehicle surface according to Ref. [25] is calculated by

$$\dot{q}_{S-G} = \dot{q}_{S-G \text{ stag}} \frac{2 \theta \sin(\theta) \left[ (1 - 1/\kappa_{\infty} M_{\infty}^2) \cos^2(\theta) + 1/\kappa_{\infty} M_{\infty}^2 \right]}{\sqrt{D}}, \quad \text{for } \theta = s/R_N < \pi/2 - \alpha \quad (45)$$

with the free stream Mach number,  $M_{\infty}$ , the free stream isentropic coefficient,  $\kappa_{\infty}$ , the length along the vehicle surface,  $s$ , the cone half angle,  $\alpha$ ,

$$D = \left( 1 - \frac{1}{\kappa_{\infty} M_{\infty}^2} \right) \left( \theta^2 - \frac{\theta \sin(4\theta)}{2} + \frac{1 - \cos(4\theta)}{8} \right) + \frac{4}{\kappa_{\infty} M_{\infty}^2} \left( \theta^2 - \theta \sin(2\theta) + \frac{1 - \cos(2\theta)}{2} \right) \dots \quad (46)$$

and

$$\dot{q}_{S-G} = \dot{q}_{S-G \text{ stag}} A \frac{s'/R_N}{\sqrt{B + (s'/R_N)^3}}, \quad \text{for } \theta = s/R_N > \pi/2 - \alpha \quad (47)$$

with

$$s' = R_N \left( \cot(\alpha) + \frac{s}{R_N} - \left( \frac{\pi}{2} - \alpha \right) \right), \quad (48)$$

$$A = \frac{\sqrt{3}}{2} \sqrt{\left(1 - \frac{1}{\kappa_\infty M_\infty^2}\right) \sin^2(\alpha) + \frac{1}{\kappa_\infty M_\infty^2} \sqrt{\frac{\pi}{2} - \alpha}} \quad (49)$$

and

$$B = \frac{3/16}{\sin^2(\alpha) \left[ \left(1 - 1/(\kappa_\infty M_\infty^2)\right) \sin^2(\alpha) + 1/(\kappa_\infty M_\infty^2) \right]} \frac{D(\theta = \pi/2 - \alpha)}{\pi/2 - \alpha} - \cot^3(\alpha). \quad (50)$$

### Van Driest's model for heat flux on flat plate geometries

The laminar non-dimensional heat transfer [27] to a flat plate is calculated based on the Stanton number correlation

$$St = \frac{c_f}{2Pr^{0.5}} \quad (51)$$

with the Blasius solution

$$c_f = \frac{0.664}{\sqrt{Re_x}} \quad (52)$$

and the recovery factor

$$r = \sqrt{Pr}. \quad (53)$$

The turbulent correlations used are repeated from Ref. [20] with

$$\begin{aligned} r = Pr_t & \left[ 1 + \frac{2}{K} \sqrt{\frac{c_f}{2}} (1 - Pr_t) \left[ \frac{\pi^2}{6} + \frac{3}{2} (1 - Pr_t) \right] + 25 \frac{c_f}{2} \left[ \left( \frac{Pr}{Pr_t} - 1 \right) + 2 \ln \left( 1 + \frac{5}{6} \left( \frac{Pr}{Pr_t} - 1 \right) \right) \right] \right. \\ & \left. + \ln 6 \cdot \ln \left( 1 + \frac{7}{8} \left( \frac{Pr}{Pr_t} - 1 \right) \right) - \ln 6 \cdot \ln \left( 1 + \frac{1}{4} \left( \frac{Pr}{Pr_t} - 1 \right) \right) \right], \end{aligned} \quad (54)$$

with the turbulent Prandtl  $Pr_t = 0.85$  [20] and  $K = 0.4$ . The Stanton number is calculated via

$$St = \frac{c_f}{2s}, \quad (55)$$

with

$$s = Pr_t \left[ 1 + \left( \frac{1 - Pr_t}{5K} \left[ \frac{\pi^2}{6} + \frac{3}{2} (1 - Pr_t) \right] + \left( \frac{Pr}{Pr_t} - 1 \right) + \ln \left( 1 + \frac{5}{6} \left( \frac{Pr}{Pr_t} - 1 \right) \right) \right) 5 \sqrt{\frac{c_f}{2}} \right], \quad (56)$$



and

$$\frac{0.242}{\sqrt{c_f(\frac{\kappa-1}{2}M_\infty^2)}}(\sin^{-1}\alpha + \sin^{-1}\beta) = 0.41 + \log_{10}(Re_{xc_f}) - 0.5 \log_{10}\left(\frac{T_w}{T_\infty}\right), \quad (57)$$

with

$$\alpha = \frac{2A^2 + B}{\sqrt{B^2 + 4A^2}}, \quad \beta = \frac{B}{\sqrt{B^2 + 4A^2}}, \quad A^2 = \frac{\kappa-1}{2}M_\infty^2 \frac{T_\infty}{T_w}, \quad B = \left(1 + \frac{\kappa-1}{2}M_\infty^2\right) \frac{T_\infty}{T_w} - 1. \quad (58)$$

### Kutateladze's model for film effectiveness downstream of an injection location

The film effectiveness is calculated using

$$\eta = \frac{1}{1 + (c_{p,g}/c_{p,f}) (0.33(4 + \xi)^{0.8} - 1)}, \quad \xi = \frac{s_{\text{from injector}}}{F \cdot W} \left( \frac{Re_f^i \mu_f^i}{\mu^*} \right)^{-0.25} \frac{\rho_g^*}{\rho_g}, \quad Re_f^i = \frac{\rho_f^i v_f^i W}{\mu_f^i}, \quad (59)$$

with the distance along the vehicle's surface from the injection point,  $s_{\text{from injector}}$ , the streamwise length of the injector,  $W$ , and the dynamic viscosity,  $\mu$  [18]. Values denoted by (\*) are evaluated at the temperature

$$T^* = 0.28 T_g + 0.72 T_{r,g} \quad (60)$$

and the values denoted by (i) are evaluated at the injection temperature,  $T_{\text{injected coolant}}$ , of Eq. (6).

### Acknowledgments

The authors would like to extend their gratitude toward James Merrifield of Fluid Gravity Engineering for his input and encouragement to perform this study. Furthermore, the help and counsel of Hannah Böhrk of DLR Stuttgart is acknowledged. The funding by EPSRC (Reference: EP/P000878/1) is greatly acknowledged. The authors would also like to extend their gratitude towards the reviewers who improved the quality of this work.

### References

- [1] Anderson, J. D., *Hypersonic and High-Temperature Gas Dynamics, Second Edition*, AIAA Education Series, 2006.
- [2] Dittert, C., Selzer, M., and Böhrk, H., "Flowfield and Pressure Decay Analysis of Porous Cones," *AIAA Journal*, Vol. 55, No. 3, 2018, pp. 874–882. doi:10.2514/1.j055298, URL <https://doi.org/10.2514/1.j055298>.
- [3] Esser, B., Gülhan, A., Reimer, T., and Petkov, I., "Experimental Verification of Thermal Management Concepts for Space Vehicles," *8th European Symposium on Aerothermodynamics for Space Vehicles*, 2015, pp. 1–8. URL <http://elib.dlr.de/97963/>.
- [4] Mohammed Ibrahim, S., Vivek, P., and Reddy, K. P. J., "Experimental Investigation on Transpiration Cooling Effectiveness for

- Spacecraft Entering Martian Atmosphere,” *AIAA Journal*, Vol. 54, No. 9, 2016, pp. 2922–2926. doi:10.2514/1.j054757, URL <https://doi.org/10.2514/1.J054757>.
- [5] Böhrk, H., “Transpiration-Cooled Hypersonic Flight Experiment: Setup, Flight Measurement, and Reconstruction,” *Journal of Spacecraft and Rockets*, Vol. 52, No. 3, 2015, pp. 674–683. doi:10.2514/1.a33144, URL <https://doi.org/10.2514/1.A33144>.
- [6] Kuhn, M., and Hald, H., “Application of Transpiration Cooling for Hot Structures,” *RESPACE - Key Technologies for Reusable Space Systems*, edited by A. Gülhan, Springer Berlin Heidelberg, Berlin, Heidelberg, 2008, pp. 82–103.
- [7] Liu, Y.-Q., Jiang, P., Jin, S.-S., and Sun, J.-G., “Transpiration cooling of a nose cone by various foreign gases,” *International Journal of Heat and Mass Transfer*, Vol. 53, 2010, pp. 5364–5372.
- [8] Basore, K. D., Selzer, M., Wheatley, V., Boyce, R. R., Mee, D. J., Capra, B. R., Kuhn, M., and Brieschenk, S., “Performance comparison of distributed injection methods for hypersonic film-cooling,” *20th Australasian Fluid Mechanics Conference*, Australasian Fluid Mechanics Society, Perth, WA, 2016. URL <https://eprints.qut.edu.au/103495/>.
- [9] Langener, T., Wolfersdorf, J. V., and Steelant, J., “Experimental Investigations on Transpiration Cooling for Scramjet Applications Using Different Coolants,” *AIAA Journal*, Vol. 49, No. 7, 2011, pp. 1409–1419. doi:10.2514/1.j050698, URL <https://doi.org/10.2514/1.J050698>.
- [10] Tanno, H., Komuro, T., Itoh, K., Kuhn, M., Petkov, I., and Esser, B., “Transpiration cooling experiments in free-piston shock tunnel HIEST,” *8th European Workshop on Thermal Protection Systems and Hot Structures*, 2016. URL <http://elib.dlr.de/105525/>.
- [11] Kays, W. M., “Heat transfer to the transpired turbulent boundary layer,” *International Journal of Heat and Mass Transfer*, Vol. 15, No. 5, 1972, pp. 1023–1044. URL <http://www.sciencedirect.com/science/article/pii/0017931072902372>.
- [12] Jiang, P., Yu, L., Sun, J.-G., and Wang, J., “Experimental and numerical investigation of convection heat transfer in transpiration cooling,” *Applied Thermal Engineering*, Vol. 24, 2004, pp. 1271–1289.
- [13] Guelhan, A., and Braun, S., “An experimental study on the efficiency of transpiration cooling in laminar and turbulent hypersonic flows,” *Experiments in Fluids*, Vol. 50, No. 3, 2011, pp. 509–525. URL <https://doi.org/10.1007/s00348-010-0945-6>.
- [14] Foreest, A. V., Sippel, M., Gülhan, A., Esser, B., C. Ambrosius, B. A., and Sudmeijer, K., “Transpiration Cooling Using Liquid Water,” *Journal of Thermophysics and Heat Transfer*, Vol. 23, No. 4, 2009, pp. 693–702. doi:10.2514/1.39070, URL <https://doi.org/10.2514/1.39070>.
- [15] Rubesin, M. W., “The influence of surface injection on heat-transfer and skin friction associated with the high-speed turbulent boundary layer,” Tech. Rep. NACA-RM-A55L13, NASA Ames Aeronautical Laboratory, 1956.
- [16] Rubesin, M. W., and Pappas, C. C., “An Analysis of the Turbulent Boundary-layer Characteristics on a Flat Plate with Distributed Light-gas Injection,” Tech. Rep. NACA-TN-4149, NASA Ames Aeronautical Laboratory, 1958.

- [17] Okuno, A. F., and Pappas, C. C., “Heat-transfer measurement for binary gas laminar boundary layers with high rates of injection,” Tech. Rep. NASA-TN-D-2473, NASA Ames Research Center, 1964.
- [18] Volchkov, E. P., Zaulichnyi, E. G., Kutateladze, S. S., and Leont’ev, A. I., “Film cooling by injection into a turbulent boundary layer,” *Journal of Applied Mechanics and Technical Physics*, Vol. 8, No. 2, 1967, pp. 63–64. URL <https://doi.org/10.1007/BF00918038>.
- [19] Kuhn, M., Hald, H., Gülhan, A., Esser, B., and Olivier, H., “Experimental Investigations of Transpiration Cooled CMC’s in Supersonic Plasma Flows,” *European Space Agency, (Special Publication) ESA SP*, Vol. 631, 2006, pp. 1–8.
- [20] Boehrk, H., Piol, O., and Kuhn, M., “Heat Balance of a Transpiration-Cooled Heat Shield,” *Journal of Thermophysics and Heat Transfer*, Vol. 24, No. 3, 2010, pp. 581–588. doi:10.2514/1.47172, URL <https://doi.org/10.2514/1.47172>.
- [21] Brune, A., Hosder, S., Gulli, S., and Maddalena, L., “Variable Transpiration Cooling Effectiveness in Laminar and Turbulent Flows for Hypersonic Vehicles,” *AIAA Journal*, Vol. 53, No. 1, 2015, pp. 176–189. doi:10.2514/1.j053053, URL <https://doi.org/10.2514/1.J053053>.
- [22] Gupta, R. N., “Aerothermodynamic Analysis of Stardust Sample Return Capsule with Coupled Radiation and Ablation,” *Journal of Spacecraft and Rockets*, Vol. 37, No. 4, 2000, pp. 507–514. doi:10.2514/2.3592, URL <https://doi.org/10.2514/2.3592>.
- [23] Johnston, C. O., Gnoffo, P. A., and Sutton, K., “Influence of Ablation on Radiative Heating for Earth Entry,” *Journal of Spacecraft and Rockets*, Vol. 46, No. 3, 2009, pp. 481–491. doi:10.2514/1.40290, URL <https://doi.org/10.2514/1.40290>.
- [24] Sutton, K., and Graves, R., “A general stagnation-point convective heating equation for arbitrary gas mixtures,” Tech. Rep. NASA TR R-376, NASA Langley Research Center, Dec. 1971.
- [25] Lees, L., “Laminar Heat Transfer Over Blunt-Nosed Bodies at Hypersonic Flight Speeds,” *Journal of Jet Propulsion*, Vol. 26, No. 4, 1956, pp. 259–269. doi:10.2514/8.6977, URL <https://doi.org/10.2514/8.6977>.
- [26] Gordon, S., and McBride, B., “Computer program for calculation of complex chemical equilibrium compositions and applications,” Tech. Rep. NASA-RP-1311, NASA Lewis Research Center, 1994.
- [27] Van Driest, E. R., “Investigation of Laminar Boundary Layer in Compressible Fluids Using the Crocco Method,” Tn-2597, NACA, 1952.
- [28] Kays, W., Crawford, M., , and Weigand, B., *Convective Heat and Mass Transfer, 4th ed.*, McGraw–Hill, New York, 2005.
- [29] Goldstein, R. J., and Jabbari, M. Y., “Film cooling effectiveness with helium and refrigerant 12 injection into a supersonic flow,” *AIAA Journal*, Vol. 8, No. 12, 1970, pp. 2273–2274. doi:10.2514/3.6100, URL <https://doi.org/10.2514/3.6100>.
- [30] Sellers, J. P., “Gaseous Film Cooling with Multiple Injection Stations,” *AIAA Journal*, Vol. 1, No. 9, 1963, pp. 2154–2156. doi:10.2514/3.2014, URL <https://doi.org/10.2514/3.2014>.

- [31] Mayer, B., Gomma, H., Weigand, B., and Zudin, Y. B., "An analytical model to evaluate heat transfer characteristics in porous media by a periodic quasi steady-state technique," *ISROMAC 2012 - 14th International Symposium on Transport Phenomena and Dynamics of Rotating Machinery*, 2012.
- [32] Schweikert, S., von Wolfersdorf, J., Selzer, M., and Hald, H., "Characterization of Actively Cooled Porous C/C Wall Segments According to Pressure Loss and Internal Temperature Distribution," *7th European Workshop on Thermal Protection Systems & Hot Structures*, 2013. URL <http://elib.dlr.de/86614/>.
- [33] Gaver, D. P., "Observing Stochastic Processes, and Approximate Transform Inversion," *Operations Research*, Vol. 14, No. 3, 1966, pp. 444 – 459.
- [34] Stehfest, H., "Algorithm 368: Numerical Inversion of Laplace Transforms [D5]," *Commun. ACM*, Vol. 13, No. 1, 1970, pp. 47–49. doi:10.1145/361953.361969, URL <http://doi.acm.org/10.1145/361953.361969>.
- [35] Hermann, T., McGilvray, M., and Ifti, H. S., "Fluid-Solid Heat Exchange in Porous Media for Transpiration Cooling Systems," *AIAA Science and Technology Forum and Exposition*, San Diego, California, 2019.
- [36] Oldfield, M., "Impulse Response Processing of Transient Heat Transfer Gauge Signals," *Journal of Turbomachinery*, Vol. 130, No. 021023, 2008. doi:10.1115/1.2752188.
- [37] Beck, J. V., Blackwell, B., and Charles R. St. Clair, J., *Inverse Heat Conduction: Ill-Posed Problems*, Wiley-Interscience, 1985.
- [38] Woodbury, K. A., and Thakur, S. K., "Redundant data and future times in the inverse heat conduction problem," *Inverse Problems in Engineering*, Vol. 2, No. 4, 1996, pp. 319–333. doi:10.1080/174159796088027610, URL <https://doi.org/10.1080/174159796088027610>.
- [39] Beck, J. V., "Nonlinear estimation applied to the nonlinear inverse heat conduction problem," *International Journal of heat and mass transfer*, Vol. 13, No. 4, 1970, pp. 703–716.
- [40] Florio, J., Henderson, J. B., Test, F. L., and Hariharan, R., "Characterization of Forced Convection Heat Transfer in Decomposing, Glass-Filled Polymer Composites," *Journal of Composite Materials*, Vol. 25, No. 11, 1991, pp. 1515–1539. doi:10.1177/002199839102501108, URL <https://doi.org/10.1177/002199839102501108>.
- [41] E. Kaattari, G., "Effects of mass addition on blunt-body boundary-layer transition and heat transfer," Tech. Rep. 1139, NASA Ames Research Center, Feb. 1978.
- [42] Thompson, R., and Gnoffo, P., "Implementation of a Blowing Boundary Condition in the LAURA Code," No. 0 in *Aerospace Sciences Meetings, American Institute of Aeronautics and Astronautics*, 2012. doi:10.2514/6.2008-1243, URL <https://doi.org/10.2514/6.2008-1243>.
- [43] Gülhan, A., Siebe, F., Thiele, T., Neeb, D., Turner, J., and Ettl, J., "Sharp Edge Flight Experiment-II Instrumentation Challenges and Selected Flight Data," *Journal of Spacecraft and Rockets*, , No. 51, 2014, pp. 175–186. URL <https://elib.dlr.de/95440/>.